with a uniform standard deviation of 5 Λ/100. To study the DFG conversion efficiency as a function of the sample thickness L, the samples are bevelled by mechanical polishing to produce wedges with angles of 25° for the recrystallized samples and 37° for the unprocessed ones.

For the DFG experiment, the pump source is a 100-mJ, 30-Hz, 1.06-μm pumped $LiNbO_3$ type I optical parametric oscillator with signal and idler waves tunable between 1.8 and 2.4 μm, yielding an 8–12-μm DFG field. See ref. 19, where a similar set-up has been used to measure DFG coherence length in ZnSe ($\sim$78 μm in the 8–12-μm DFG range)[19]. If a resonance is to be found, it is thus expected for a grain size of about 78 μm. This large value of the coherence length originates from the minimum index dispersion of ZnSe in this spectral region equidistant between the gap and the Restrahlung energies. This explains the large nonlinear yields expected in ZnSe polycrystalline materials, as expected from equations (1) to (4). About 200 μJ of the available energy are focused to a waist of about 200 μm in the samples. The bevelled samples are translated on a motorized mount. The DFG wave energy is measured using a HgCdTe cryogenic detector protected by adequate filters.

We first studied the variation of the DFG signal as a function of the sample thickness. To explore a large thickness range, we chose the 37° wedged sample. Figure 2 shows the variation of the measured signal as a function of the crystal thickness. The signal was normalized to the signal obtained in the same configuration by a DFG signal due to a signal coherence length (as determined in a crystalline $\langle 110 \rangle$ wedge sample[19]). Clearly, the signal follows the expected linear dependence on sample length L. Given the experimental values $\Lambda/\Lambda_c \approx 0.38$, $\sigma_x/\Lambda \approx 5\%$ and $\langle d^2 \rangle / d^2 \approx 14\%$, equation (4) predicts a $N_{\rm eff}/N$ ratio of 4.5%, whereas a ratio of 2.8% is experimentally determined from Fig. 2, which is the right order of magnitude.

We then studied the influence of the grain size on the DFG signal. The preceding experiment was performed for each of the three SPR samples. Linear variations as a function of the sample thickness were observed in all the samples. Figure 3 shows the theoretical and experimental values of the normalized efficiency for the four different values of the grain mean size Λ, taking into account an experimentally determined loss term of $\rho = 4.5\%\ {\rm cm}^{-1}$. This loss is due to a very small amount of light scattering (corresponding to a mean free path for $\sim$2-μm photons of 22 cm), a situation which is fundamentally different from previous work[14]. The observed variations are in good agreement with the theoretical predictions. Finally, we study the variation of the DFG signal as a function (1) of the orientation of the pump polarization relative to the sample bevel direction, (2) of the angle between the pump and the DFG beam polarization, and (3) of the two pump frequencies. No significant variation of the DFG signal could be observed in any of these experiments, which confirms the absence of crystallographic texture in our samples.

Random quasi-phase-matching may then become a valuable building block in nonlinear optics. Such materials can be deposited on any substrate (such as silicon) with no particular restrictions regarding crystalline growth or sample length, opening the way to optical conversion in low-cost deposited waveguides. Its extremely loose frequency selectivity makes it of particular interest for generating optical radiations with ultra-wide spectral tunability and reasonable efficiency. It may also be applied to emerging materials such as ZnO, chromium-doped ZnSe or new laser ceramics, allowing multifunctional materials to be developed.

We note that, although quasi-phase-matched GaAs crystals have been demonstrated to be far more efficient nonlinear optical converters in the 8–12 μm range[8,9,20], these crystals have not yet been demonstrated over large lengths. But large size samples are available in polycrystalline materials (commonly > 100 mm for the ZnSe samples), so that good conversion yields could eventually be reached. This, added to the extreme ease-of-use of the random quasi-phase-matching technique (almost no control is needed), makes of any piece of polycrystalline ZnSe a cheap and efficient optical converter. ☐

Received 3 May; accepted 22 September 2004; doi:10.1038/nature03027.

1. Armstrong, J. A., Bloembergen, N., Ducuing, J. & Pershan, P. S. Interactions between light waves in a nonlinear dielectric. *Phys. Rev.* **127,** 1918–1939 (1962).
2. Rosencher, E. & Vinter, B. *Optoelectronics* (Cambridge Univ. Press, Cambridge, 2002).
3. Morozov, E. Y., Kaminskii, A. A., Chirkin, A. S. & Yusupov, D. B. Second optical harmonic generation in non linear crystals with a disordered domain structure. *JETP Lett.* **73,** 647–650 (2001).
4. Fejer, M. M. Nonlinear optical frequency conversion. *Phys. Today* **40,** 25–32 (1994).
5. Ebrahimzadeh, M. & Dunn, M. H. Parametric generation of tunable light from continuous-wave to femtosecond pulses. *Science* **286,** 1513–1517 (1999).
6. Fiore, A., Berger, V., Rosencher, E., Bravetti, P. & Nagle, J. Phase matching using an isotropic nonlinear optical material. *Nature* **391,** 463–466 (1998).
7. Rosencher, E. *et al.* Quantum engineering of optical nonlinearities. *Science* **271,** 168–173 (1996).
8. Levi, O. *et al.* Difference frequency generation of 8-μm radiation in orientation-patterned GaAs. *Opt. Lett.* **27,** 2091–2093 (2002).
9. Eyres, L. A. *et al.* All-epitaxial fabrication of thick, orientation-patterned GaAs films for nonlinear optical frequency conversion. *Appl. Phys. Lett.* **79** (2001).
10. Fejer, M. M., Magel, G. A., Jundt, D. H. & Byer, R. L. Quasi-phase-matched second harmonic generation: tuning and tolerances. *IEEE J. Quant. Electron.* **28,** 2631–3654 (1992).
11. Agranovitch, V. M. & Kravtsov, V. E. Nonlinear backscattering from opaque media. *Phys. Rev. B* **43,** 13691–13694 (1991).
12. Kravtsov, V. E., Agranovitch, V. M. & Grigorishin, K. I. Theory of second-harmonic generation in strongly scattering media. *Phys. Rev. B* **44,** 4931–4942 (1991).
13. Makeev, E. V. & Skipetrov, S. E. Second harmonic generation in suspensions of spherical particles. *Opt. Commun.* **224,** 139–147 (2003).
14. Mel'nikov, V. A. *et al.* Second-harmonic generation in strongly scattering porous gallium phosphide. *Appl. Phys. B* **79,** 225–228 (2004).
15. Wiersma, D. S. & Cavalieri, S. A temperature-tunable random laser. *Nature* **414,** 708–709 (2002).
16. Kurtz, S. K. & Perry, T. T. A powder technique for the evaluation of non linear optical materials. *J. Appl. Phys.* **39,** 3798–3813 (1968).
17. Shoji, I., Kondo, T., Kitamoto, A., Shirane, M. & Ito, R. Absolute scale of second-order nonlinear-optical coefficients. *J. Opt. Soc. Am. B* **14,** 2268–2294 (1997).
18. Rzepka, E., Roger, J. P., Lemasson, P. & Triboulet, R. Optical transmission of ZnSe crystals grown by solid phase recrystallisation. *J. Cryst. Growth* **197,** 480–484 (1999).
19. Haidar, R. *et al.* Largely tunable mid-infrared (8–12 μm) difference frequency generation in isotropic semiconductors. *J. Appl. Phys.* **91,** 2550–2552 (2002).
20. Vodopyanov, K. L. *et al.* Optical parametric oscillation in quasi-phase-matched GaAs. *Opt. Lett.* **29,** 1912–1914 (2004).

Acknowledgements We are indebted to C. Sanchez and A. Cheniere for X-ray measurements, A. Godard, M. Lefebvre and N. Guérineau for help, to M. Fejer for discussions, and D. Sessler for critical reading of the manuscript. This work was supported by the Délégation Générale pour l'Armement (DGA).

Competing interests statement The authors declare that they have no competing financial interests.

Correspondence and requests for materials should be addressed to E. R. (rosencher@onera.fr).

Metal wires for terahertz wave guiding

Kanglin Wang & Daniel M. Mittleman

Department of Electrical and Computer Engineering, MS 366, Rice University, Houston, Texas 77251-1892, USA

Sources and systems for far-infrared or terahertz ($1\ {\rm THz} = 10^{12}\ {\rm Hz}$) radiation have received extensive attention in recent years, with applications in sensing, imaging and spectroscopy[1–10]. Terahertz radiation bridges the gap between the microwave and optical regimes, and offers significant scientific and technological potential in many fields. However, waveguiding in this intermediate spectral region still remains a challenge. Neither conventional metal waveguides for microwave radiation, nor dielectric fibres for visible and near-infrared radiation can be used to guide terahertz waves over a long distance, owing to the high loss from the finite conductivity of metals or the high

absorption coefficient of dielectric materials in this spectral range. Furthermore, the extensive use of broadband pulses in the terahertz regime imposes an additional constraint of low dispersion, which is necessary for compatibility with spectroscopic applications. Here we show how a simple waveguide, namely a bare metal wire, can be used to transport terahertz pulses with virtually no dispersion, low attenuation, and with remarkable structural simplicity. As an example of this new waveguiding structure, we demonstrate an endoscope for terahertz pulses.

In an attempt to meet the compelling need for useful THz waveguides, various guides with quasi-optical coupling have been demonstrated within the last few years. Most of these have been based on conventional guiding structures, such as metal tubes[11,12], plastic ribbons[13] or dielectric fibres[14]. There have also been reports on the application of the latest technology of photonic crystal fibres to THz radiation[15,16]. In all of these cases, the utility for transport of THz pulses is limited not only by the high loss, but also by group velocity dispersion of the guided waves. The most promising studies have reported dispersionless propagation in parallel metal plate waveguides[17–19]. But in this case the attenuation is still unacceptably high, due in large part to the finite conductivity of the metal plates. In addition, the cross-sectional area of the waveguide is too large for many of the proposed THz applications, including in particular medical diagnostics.

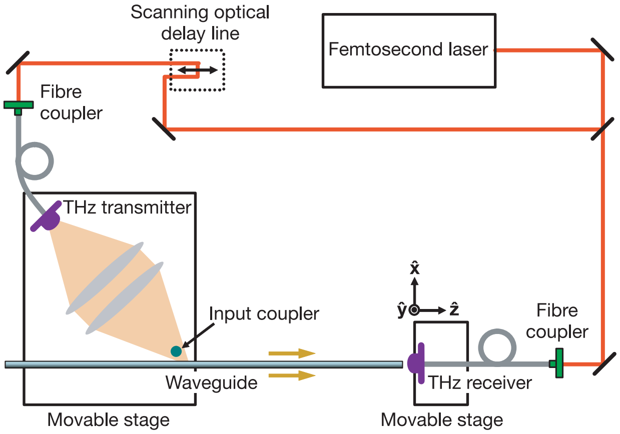

Figure 1 A diagram of the optical set-up for characterizing the propagating electromagnetic mode on a metal wire waveguide. Horizontally polarized THz pulses are generated by a fibre-coupled photoconductive transmitter and focused onto a stainless steel waveguide with a diameter of 0.9 mm. A second stainless steel wire is placed at the focal spot, oriented perpendicular to the waveguide, to act as an input coupler. A radially polarized mode is excited in the space around the waveguide. The electric field of the propagating pulses is detected at the end of the waveguide with a fibre-coupled photoconductive receiver, which is sensitive only to the vertical polarization component. The transmitter, the focusing lenses, and the coupler are all mounted on a movable stage which can be moved along the waveguide. The receiver is mounted on a stage which can be moved in three dimensions relative to the end of the waveguide.

Our interest in the wire geometry was motivated by our recent studies of the propagation of THz pulses on optical antennas in near-field scanning optical microscopy (NSOM)[20]. Here, with the direct measurement of the electric field in the time domain, we show that the guided mode on a metal wire is similar to the transverse electromagnetic (TEM) mode of a conventional coaxial waveguide, and exhibits all of the properties required for a practical far-infrared waveguide. Because of the low exposed metal surface area of these wire waveguides, the attenuation due to conductivity losses are substantially lower than any previously reported structure. Based on these unique properties, we have realized a Y-splitter and a 90° output directing structure, and have constructed the first endoscope for THz pulses.

In our experiment, the broadband single-cycle pulses of free-space THz radiation are generated and coherently detected using ultrafast photoconductive sampling[2,3] with fibre-coupled THz antennas[21]. A diagram of the experimental set-up is shown in Fig. 1. The horizontally polarized THz pulses are focused onto the stainless steel waveguide. A second stainless steel wire is placed at the focal spot, oriented perpendicular to the waveguide (that is, out of the page in Fig. 1). This second wire serves as an input coupler. Scattering of the input THz radiation at the intersection structure helps to excite a propagating waveguide mode, with a radially polarized mode pattern. Both the waveguide and the coupler are 0.9 mm in diameter, and the separation between them is 0.5 mm. The receiver is placed at the end of the waveguide, and is oriented to detect only the vertically polarized component of the electric field in order to eliminate the possibility of detecting directly scattered radiation which would interfere with the detection of the guided mode. The incident THz beam is modulated by a chopper in front of the transmitter, and a lock-in amplifier is used for detecting the induced photocurrent in the receiver. The THz transmitter, the focusing lenses, and the coupler are all mounted on a movable stage so that the incident position along the waveguide can be controlled. The THz receiver is mounted on a three-axis stage for detection at various positions relative to the end of the waveguide.

Figure 2a shows typical time-domain electric field waveforms, for two different receiver positions located symmetrically above and below the wire waveguide. These waves are vertically (y) polarized, perpendicular to the horizontally (x) polarized input beam. The polarity reversal as the detector scans across the wire clearly shows the radially polarized nature of the guided wave. To observe the spatial profile of the mode, we scan the receiver in a plane perpendicular to the waveguide axis, with a time delay fixed at the

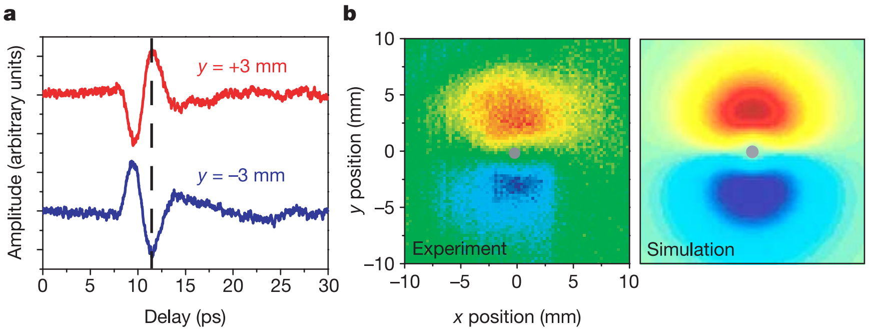

Figure 2 Spatial mode of the guided wave on a metal wire. **a**, Time-domain electric field waveforms detected with the receiver 3 mm above and 3 mm below the waveguide. The polarity reversal is an indication of the radial nature of the polarization. **b**, Left panel: spatial profile of the electric field obtained by moving the THz receiver in a plane perpendicular to the waveguide axis. The time delay is fixed at the peak of the THz pulses indicated by the dashed line in **a**. Red represents positive values and blue represents negative values. The simulation (right panel) shows the vertical component of the electric field for a cylindrically symmetric radial mode.

peak of the THz pulses. Because the detector is sensitive only to one polarization, it is not possible to directly detect the spatial distribution of a radially polarized mode. Instead, the measured mode should resemble the projection of a cylindrically symmetric radial mode onto the vertical (y) direction. We simulate this effect by first computing the two-dimensional field distribution of a radial mode and then projecting it onto a single polarization axis. This simulation is in good agreement with the data (see Fig. 2b and also ref. 22).

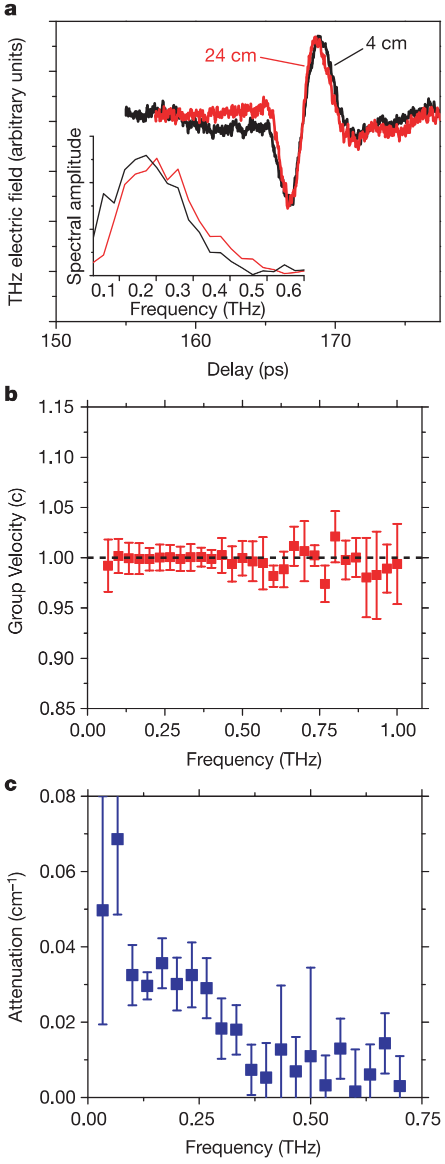

Figure 3 Characteristics of the propagating mode. **a**, THz waveforms measured after 4 cm (black) and 24 cm (red) of propagation distance along the wire. In order to compare the shapes of these two waveforms, the red curve has been shifted by 667.9 ps along the time axis, so that it coincides with the black curve. In addition, it has been multiplied by a factor of 1.6, which corresponds to an amplitude attenuation coefficient of less than 0.03 cm^{-1}. The propagation is essentially dispersionless. The red curve is slightly narrower, indicating that the high frequency components are attenuated slightly less than the low frequency components. This is also clear from the normalized amplitude spectra of the two waveforms, shown in the inset. **b**, Group velocity of the propagating mode as a function of frequency, derived from a series of measurements with different propagation distances. **c**, The electric field amplitude attenuation coefficient of the propagating mode as a function of frequency, derived in the same manner as in **b**. As anticipated from **a**, this loss decreases with increasing frequency, in contrast to other THz waveguides in which the loss is dominated by finite conductivity effects. In **b** and **c**, error bars show ±1 s.d.

We characterize the propagation of this radial mode by moving the incident position of the THz beam along the waveguide. There is no evident change in the shape of the time-domain waveforms for propagation distances up to 24 cm, showing that this propagation is largely dispersionless (see Fig. 3a). By analysing the spectra of these waveforms, we can derive the group velocity, v_g, and the electric field amplitude attenuation coefficient, α, as a function of frequency. These results are shown in Fig. 3b and c. The radial nature of the mode, combined with the absence of group velocity dispersion throughout the measurable spectral range, suggests that the propagating mode has the characteristics of the lowest-order (TEM) mode of a coaxial waveguide. The average attenuation coefficient, weighted by the pulse power spectrum, is less than 0.03 cm^{-1}, the lowest of any THz waveguide reported to date[19].

This low attenuation emphasizes one unique aspect of the wire waveguide. Compared to other waveguide geometries, a metal wire has a much smaller surface area interacting with the electromagnetic field, so the propagation loss due to finite conductivity of the metal is negligible[23]. Instead, the measured radiative losses arise from diffractive spreading of the propagating mode in the lateral dimensions. This distinction can be seen by noting that, as shown in Fig. 3, the losses decrease with increasing frequency, in contrast to the case of waveguides in which the loss is dominated by ohmic effects[18]. This frequency dependence may arise from the overlap between the guided mode and propagating far-field modes. We note that our measurements do not reflect the losses associated with the coupling of the free-space THz beam to the guided mode; in the experiment described here, these losses are quite large. In addition, our coupling mechanism probably excites a superposition of guided modes, which may lead to larger diffractive losses due to the higher transverse spatial frequencies that comprise higher-order coaxial modes. More effective mode-matching will be important to optimize both the input coupling and the propagation losses[12,24].

We observe that the guided mode can propagate on a slightly curved waveguide without a substantial increase in the loss. It is also found that the guided propagation can be easily coupled between two curved waveguides in contact with each other (or between a curved waveguide and a straight one). These features enable a very simple scheme for a beam splitter, as illustrated in Fig. 4. Another remarkable feature of the metal wire waveguide is that the mode maintains its radial nature as it propagates off the end of the

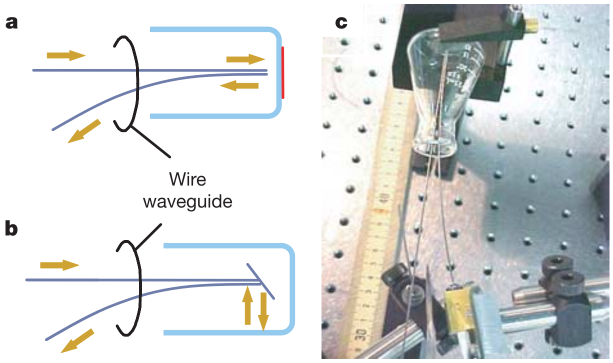

Figure 4 The THz endoscope. **a**, The optical configuration for a THz endoscopic measurement of a region at the bottom of a cavity. The input pulses are launched to the detection region with a straight waveguide. By using a Y-splitter structure, the reflected pulses are directed to a branch waveguide for detection. The red bar indicates a metal plate affixed to the exterior of the cavity, to enhance the reflection from this dielectric interface. **b**, The optical configuration for a THz endoscopic measurement of the side wall in a cavity. The input pulses are launched by a straight waveguide, and directed off the waveguide perpendicularly by a small mirror attached at the distal end of the endoscope. The reflected pulses go back to the waveguide after the reflection at the distal mirror, and are then directed to the output waveguide by a Y-splitter. **c**, Photograph of a THz endoscope which is inserted into a flask, for a measurement with the configuration shown in **a**.

waveguide, for at least several centimetres. As a result, we can build a 90° output director by attaching a small mirror at the end of the waveguide, tilted at a 45° angle with respect to the axis of the waveguide. With these two structures realized, we construct a THz endoscope based on the wire waveguide. Endoscopic measurements can be performed by inserting the distal end of the endoscope (with attached mirror) into any container. Two such configurations are shown in Fig. 4.

Figure 5 shows the results of demonstration experiments performed in these two configurations. In each case, we display a pair of waveforms measured on either side of the waveguide, as in Fig. 2a. In Fig. 5a, the two reflections in each waveform arise from the two dielectric interfaces at the bottom of the glass flask. By attaching a piece of metal to the flask bottom, the strength of the second reflection is enhanced. Another experiment (Fig. 5b) is the measurement of a reflection from the side wall of a metal tube into which the endoscope has been inserted, as in Fig. 4b. In this case, the signal is not as strong as in the previous measurement owing to the additional propagation and coupling processes.

The low loss and negligible group velocity dispersion make this new type of waveguide especially suitable for use in THz research and applications. Our results also show that it is now possible to direct THz pulses inside containers or around corners, where line-of-sight optical access is not practical. In addition, we can launch THz pulses along any thin metal rod structures. In situations where the guided mode could be perturbed by other structures close to the waveguide, a section of outer metallic shield could be added to form a coaxial waveguide, as long as the additional ohmic losses can be tolerated. A THz endoscope has been successfully constructed to demonstrate the use of the metal wire waveguide, which paves the way for a wide range of new applications for terahertz sensing and imaging. ☐

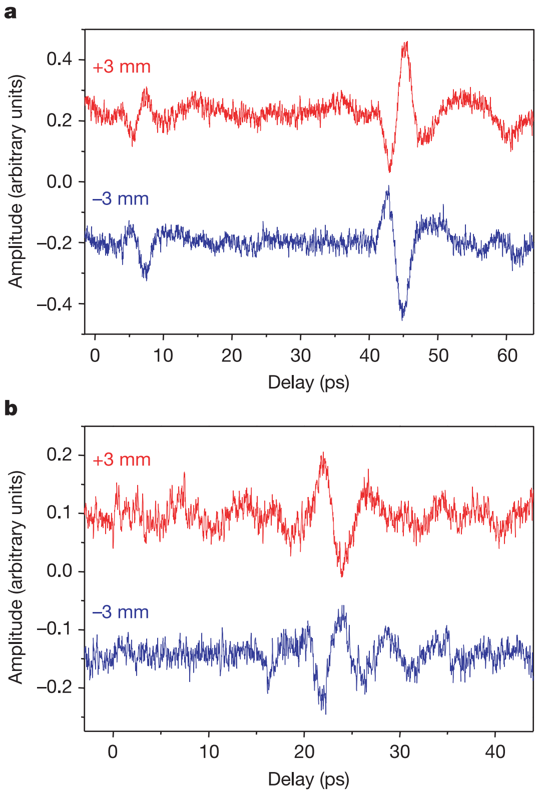

Figure 5 Endoscopic measurements. **a**, THz waveforms obtained with the receiver 3 mm above and 3 mm below the end of the output waveguide, in the experiment depicted in Fig. 4c. The two pulses in each waveform arise from the reflections at the two dielectric interfaces at the bottom of the glass flask. The enhancement of the second pulse is due to a metal plate attached to the flask bottom. **b**, THz waveforms obtained in a measurement with the configuration of Fig. 4b, by inserting the endoscope with an end directing mirror into a metal tube. The relatively weak signal results from the additional propagation and coupling process of THz pulses at the distal end of the endoscope.

Received 13 July; accepted 13 September 2004; doi:10.1038/nature03040.

1. Mittleman, D. (ed.) *Sensing with Terahertz Radiation* (Springer, Heidelberg, 2002).
2. Smith, P. R., Auston, D. H. & Nuss, M. C. Subpicosecond photoconducting dipole antennas. *IEEE J. Quant. Electron.* **24,** 255–260 (1988).
3. van Exter, M. & Grischkowsky, D. Characterization of an optoelectronic terahertz beam system. *IEEE Trans. Microwave Theory Tech.* **38,** 1684–1691 (1990).
4. Jepsen, P. U., Jacobsen, R. H. & Keiding, S. R. Generation and detection of terahertz pulses from biased semiconductor antennas. *J. Opt. Soc. Am. B* **13,** 2424–2436 (1996).
5. Mittleman, D. M., Jacobsen, R. H. & Nuss, M. C. T-ray imaging. *IEEE J. Select. Top. Quant. Electron.* **2,** 679–692 (1996).
6. Jacobsen, R. H., Mittleman, D. M. & Nuss, M. C. Chemical recognition of gases and gas mixtures with terahertz waves. *Opt. Lett.* **21,** 2011–2013 (1996).
7. Woodward, R. M., Wallace, V. P., Arnone, D. D., Linfield, E. H. & Pepper, M. Terahertz pulsed imaging of skin cancer in the time and frequency domain. *J. Biol. Phys.* **29,** 257–261 (2003).
8. Crawley, D. *et al.* Three-dimensional terahertz pulse imaging of dental tissue. *J. Biomed. Opt.* **8,** 303–307 (2003).
9. Kawase, K., Ogawa, Y. & Watanabe, Y. Non-destructive terahertz imaging of illicit drugs using spectral fingerprints. *Opt. Express* **11,** 2549–2554 (2003).
10. Wang, S. & Zhang, X.-C. Pulsed terahertz tomography. *J. Phys. D* **37,** R1–R36 (2004).
11. McGowan, R. W., Gallot, G. & Grischkowsky, D. Propagation of ultrawideband short pulses of THz radiation through submillimeter-diameter circular waveguides. *Opt. Lett.* **24,** 1431–1433 (1999).
12. Gallot, G., Jamison, S. P., McGowan, R. W. & Grischkowsky, D. Terahertz waveguides. *J. Opt. Soc. Am. B* **17,** 851–863 (2000).
13. Mendis, R. & Grischkowsky, D. Plastic ribbon THz waveguides. *J. Appl. Phys.* **88,** 4449–4451 (2000).
14. Jamison, S. P., McGown, R. W. & Grischkowsky, D. Single-mode waveguide propagation and reshaping of sub-ps terahertz pulses in sapphire fiber. *Appl. Phys. Lett.* **76,** 1987–1989 (2000).
15. Han, H., Park, H., Cho, M. & Kim, J. Terahertz pulse propagation in a plastic photonic crystal fiber. *Appl. Phys. Lett.* **80,** 2634–2636 (2002).
16. Goto, M., Quema, A., Takahashi, H., Ono, S. & Sarukura, N. Teflon photonic crystal fiber as terahertz waveguide. *Jpn. J. Appl. Phys.* **43,** L317–L319 (2004).
17. Mendis, R. & Grischkowsky, D. Undistorted guided-wave propagation of subpicosecond terahertz pulses. *Opt. Lett.* **26,** 846–848 (2001).
18. Mendis, R. & Grischkowsky, D. THz interconnect with low loss and low group velocity dispersion. *IEEE Microwave Wireless Comp. Lett.* **11,** 444–446 (2001).
19. Coleman, S. & Grischkowsky, D. A THz transverse electromagnetic mode two-dimensional interconnect layer incorporating quasi-optics. *Appl. Phys. Lett.* **83,** 3656–3658 (2003).
20. Wang, K., Barkan, A. & Mittleman, D. M. Propagation effects in apertureless near-field optical antennas. *Appl. Phys. Lett.* **84,** 305–307 (2004).
21. Rudd, J. V., Zimdars, D. & Warmuth, M. Compact fiber-pigtailed terahertz imaging system. *Proc. SPIE* **3934,** 27–35 (2000).
22. Quabis, S., Dorn, R., Eberler, M., Glöckl, O. & Leuchs, G. Focusing light to a tighter spot. *Opt. Commun.* **179,** 1–6 (2000).
23. Marcuvitz, N. *Waveguide Handbook* (McGraw-Hill, New York, 1951).
24. Coleman, S. & Grischkowsky, D. Parallel plate THz transmitter. *Appl. Phys. Lett.* **84,** 654–656 (2004).

Acknowledgements This work was supported in part by the R. A. Welch Foundation, the National Science Foundation and Advanced Micro Devices.

Competing interests statement The authors declare that they have no competing financial interests.

Correspondence and requests for materials should be addressed to D.M.M. (daniel@rice.edu).

Constraints on the duration and freshwater release of Heinrich event 4 through isotope modelling

D. Roche, D. Paillard & E. Cortijo

IPSL/Laboratoire des Sciences du Climat et de l'Environnement, CEA-CNRS, 91191 Gif sur Yvette, France

Heinrich events[1]—abrupt climate cooling events due to ice-sheet instability that occurred during the last glacial period—are recorded in sediment cores throughout the North Atlantic Ocean[2,3]. Modelling studies have described likely physical mechanisms[4–6] for these events, but the quantitative characteristics of

Copyright of Nature is the property of Nature Publishing Group and its content may not be copied or emailed to multiple sites or posted to a listserv without the copyright holder's express written permission. However, users may print, download, or email articles for individual use.